



HAL
open science

Terahertz pulse generation by two-color laser fields with circular polarization

C. Tailliez, A. Stathopoulos, Stefan Skupin, D. Buožius, I. Babushkin, V. Vaičaitis, L. Bergé

► **To cite this version:**

C. Tailliez, A. Stathopoulos, Stefan Skupin, D. Buožius, I. Babushkin, et al.. Terahertz pulse generation by two-color laser fields with circular polarization. *New Journal of Physics*, 2020, 22 (10), pp.103038. 10.1088/1367-2630/abb863 . hal-02901363v2

HAL Id: hal-02901363

<https://hal.science/hal-02901363v2>

Submitted on 5 Nov 2020

HAL is a multi-disciplinary open access archive for the deposit and dissemination of scientific research documents, whether they are published or not. The documents may come from teaching and research institutions in France or abroad, or from public or private research centers.

L'archive ouverte pluridisciplinaire **HAL**, est destinée au dépôt et à la diffusion de documents scientifiques de niveau recherche, publiés ou non, émanant des établissements d'enseignement et de recherche français ou étrangers, des laboratoires publics ou privés.

PAPER • OPEN ACCESS

Terahertz pulse generation by two-color laser fields with circular polarization




To cite this article: C Tailliez *et al* 2020 *New J. Phys.* **22** 103038

View the [article online](#) for updates and enhancements.



PAPER

Terahertz pulse generation by two-color laser fields with circular polarization

C Tailliez^{1,2}, A Stathopoulos^{1,2}, S Skupin^{3,*} , D Buožius⁴, I Babushkin^{5,6,7} ,
V Vaičaitis⁴  and L Berge^{1,2} 

¹ CEA, DAM, DIF, 91297 Arpajon, France

² Université Paris-Saclay, CEA, LMCE, 91680 Bruyères-le-Châtel, France

³ Institut Lumière Matière, UMR 5306 Université Lyon 1-CNRS, Université de Lyon, 69622 Villeurbanne, France

⁴ Laser Research Center, Vilnius University, Saulėtekio 10, Vilnius LT-10223, Lithuania

⁵ Institute of Quantum Optics, Leibniz University Hannover, Welfengarten 1 30167, Hannover, Germany

⁶ Cluster of Excellence PhoenixD (Photonics, Optics, and Engineering- Innovation Across Disciplines), 30167 Hannover, Germany

⁷ Max Born Institute, Max Born Str. 2a, 12489 Berlin, Germany

* Author to whom any correspondence should be addressed.

E-mail: stefan.skupin@univ-lyon1.fr

Keywords: terahertz generation, polarization control, plasma, filamentation, ultrashort pulse propagation

RECEIVED

16 July 2020

REVISED

4 September 2020

ACCEPTED FOR PUBLICATION

14 September 2020

PUBLISHED

16 October 2020

Original content from
this work may be used
under the terms of the
[Creative Commons
Attribution 4.0 licence](#).

Any further distribution
of this work must
maintain attribution to
the author(s) and the
title of the work, journal
citation and DOI.



Abstract

We study the influence of the polarization states of ionizing femtosecond two-color pulses on the emitted terahertz radiation in gases. A local-current model and plane-wave evaluations justify the previously-reported impact on the THz energy yield and a (almost) linearly-polarized THz field when using circularly-polarized laser harmonics. For such pump pulses, the THz yield is independent of the relative phase between the two colors. When the pump pulses have same helicity, the increase in the THz yield is associated with longer ionization sequences and higher electron transverse momenta acquired in the driving field. Reversely, for two color pulses with opposite helicity, the dramatic loss of THz power comes from destructive interferences driven by the highly symmetric response of the photocurrents lined up on the third harmonic of the fundamental pulse. While our experiments confirm an increased THz yield for circularly-polarized pumps of same helicity, surprisingly, the emitted THz radiation is not linearly-polarized. This effect is explained by means of comprehensive 3D numerical simulations highlighting the role of the spatial alignment and non-collinear propagation of the two colors.

1. Introduction

Terahertz (THz) waves are rapidly attracting interest due to their wide application range, both in imaging techniques and coherent spectroscopy [1–4] applied to various areas such as medical diagnostics, remote detection or cultural heritage to mention a few. In addition, energetic ($> 100 \mu\text{J}$) THz pulses with GV m^{-1} field strength open promising perspectives in the development of compact THz electron accelerators [5] and THz-triggered chemistry [6], for which relativistic plasmas may supply suitable emitters in the future [7–9]. Imaging applications usually need narrowband and up to μJ energy radiation produced by, e.g., photoconductive antennas [10, 11] or quantum cascade lasers [12]. THz-driven electron acceleration requires in turn narrowband, but more energetic (sub-mJ) emitters, currently provided by optical rectification in crystals and possibly optimized by the tilted-pulse-front technique [13, 14]. These solid-based technologies are able to supply sub-mJ, $\sim\text{GV m}^{-1}$ field strengths associated with percent-level conversion efficiencies and THz bandwidths barely exceeding ~ 5 THz. They are, however, hampered by their inherent damage threshold that may require prohibitively large crystals to be partly overcome. By contrast, gas-plasmas excited by intense, two-color femtosecond pulses at intensities close to ionization threshold $\sim 10^{14} \text{ W cm}^{-2}$ are known to provide significant conversion efficiency $> 10^{-4}$ up to the percent level [15, 16], relatively high field strength $\geq 0.1 \text{ GV m}^{-1}$ and $\sim 50\text{--}100$ THz broadband spectra [17–19]. Generally created by the combination of a fundamental harmonic (FH) and second harmonic (SH), the

generation mechanism is here the creation of photocurrents induced by the free electrons tunnel-ionized from gas molecules and being accelerated by an asymmetric two-color field [20–22]. Excited by collinearly-polarized pulse components, the measured THz power is highly sensitive to the relative phase difference ϕ between the two colors and exhibits maxima when the value of ϕ is close to $\pi/2$ (modulo π) [20, 23].

Several means for increasing the THz energy yield emitted by photocurrents have been explored. Among the laser-medium parameters exploited for this purpose, increasing the FH wavelength led to a significant growth in the THz pulse energy proportional to λ_0^{4-5} using OPCPA lasers operating between 0.8 and 2 μm [24]. Comprehensive numerical simulations of this experiment demonstrated the crucial role of the relative phase initiated along the SH generation stage through a doubling crystal (e.g., BBO) and achieved in the plasma zone [25]. More recently, the advent of sub-mJ, ultrafast mid-IR (3.9 μm) and CO₂ (10.6 μm) lasers inspired both numerical [26, 27] and experimental [15, 16] investigations confirming the increase in the conversion efficiency over 1–2% and ~ 0.1 mJ THz yields for pump energies < 10 mJ. Alternative methods for increasing the THz yield may also rely on an optimum tuning of the intensity level versus the ionized gas (e.g., Ar, He) and their successive electron shells [28], playing on the pump pulse duration or reducing the plasma dimensions [29–31], increasing the number of colors [32–34] or even modifying the frequency ratio between the two colors [35, 36]. By combining these techniques one can expect to augment the THz pulse energy by at least one order of magnitude.

Despite the proven effectiveness of the previous methods, there exists a direct means to improve the THz performances in air photonics, which consists in simply changing the polarization state of the FH and SH components. Pioneering a coherent control of THz wave generation through the polarization state of the two colors, Dai *et al* [37] experimentally reported a continuous rotation of the resulting THz field polarization, always remaining linear, and the invariance of the radiation energy yield by changing the two-color relative phase (ϕ) when using circularly-polarized (CP) pulses. The dependency of the THz pulse energy with respect to the polarization of two-color laser pulses was later thoroughly investigated by Meng *et al* [38]. Inspired by the remarkable enhancement of the electron energy driven by tunnel ionization [39], these authors experimentally evidenced from helium gas jets that CP two-color pulses with same helicity (CP-S) could deliver ~ 5 times higher THz powers than their linearly-polarized, parallel (LP-P) counterparts. Despite ionization yields being reduced for CP pulses due to a factor $1/\sqrt{2}$ in the electric field amplitude, the increase in the THz power was attributed to an ionization process saturated (for completely ionized atoms) closer to the peak of the laser electric field and associated to the highest values of the acquired electron drift velocity. By contrast, CP pulses with counter-helicity (CP-C) in their SH delivered a much weaker THz yield, remaining, in the experiments [38], of the order of that supplied by linearly-polarized (LP) pulses with orthogonally-polarized colors (LP-O). Among the four investigated polarization states (CP-S, CP-C, LP-P, LP-O), only pulses being linearly polarized underwent a strong dependency on the relative phase ϕ . Meanwhile, the effects of the pump polarization states were also investigated numerically. In [40] the influence of circularly-polarized two-color pulses driven either by four-wave mixing (FWM) or by photocurrents confirmed the previous dependencies of the resulting THz field on the two-color phase offset. In reference [41], the generation and control of elliptically-polarized THz waves was demonstrated from air plasmas driven by few-cycle CP pulses. For in-line laser focusing, the THz polarization state was experimentally found to evolve from linear to elliptical by increasing the plasma length [42]. More recently, theoretical evaluations based on an extended 3D local-current (LC) model [43] explored the role of the laser parameters (pulse duration, relative phase, tilt angle of linear polarization) on the radiation characteristics. Kosareva and co-workers [44, 45], by analyzing the polarization properties of the pulse harmonics and broadband THz generation from atmospheric plasmas, reported the decrease by about one order of magnitude of the THz yield provided by LP-O pulses compared to LP-P's. In [44], abrupt changes in the THz polarization were observed from an angle $\sim 85^\circ$ between the FH and SH polarization axis and a weak ellipticity was sufficient to drive efficiently an elliptical THz radiation.

From the numerical point of view, by solving the quantum time-dependent Schrödinger equation based on the single-atom response [37, 38, 46] it was possible to figure out partial features of the previous properties. However, we are still missing a thorough explanation of the changes induced in the characteristic laser-driven ionization steps and the electron transverse momenta by two-color pumps with different polarization states, and of their impact on the THz conversion efficiency. Such modifications can be cleared up by means of the LC model and the microscopic description of the THz spectra built up by photocurrents in the tunnel-ionization regime [47], which is one of the goals of the present work. Here, we revisit the effects of two-color laser fields with elliptical polarization on the THz yield and on the polarization state of the THz radiation. The weak THz yield obtained in LP-O configuration has already been justified by the vanishing of the (dominant) FH component in the electron density spectrum and THz radiation only conveyed by the (minor) SH component [31, 45, 48]. Therefore, emphasis will be laid on CP-S, CP-C and

LP-P pump configurations throughout the present analysis. We shall also examine the stability of both the THz energy yield and the radiation polarization state experimentally and by comprehensive numerical simulations based on a unidirectional solver [49]. In this work, we confirm and explain the high THz energy level reached when using CP-S pulses, and display evidence of the fragility of CP-C pump pulses in totally inhibiting THz emission. Special attention is further paid to the impact of the alignment of the two colors on the generated THz field and its polarization.

The paper is organized as follows. In section 2 we derive basic evaluations of vectorial THz components excited through FWM and photocurrents by CP and LP pulses and comment on their validity in regards to $(0 + 1)$ - dimensional LC computations. This analysis explains the changes in the density steps and ionization duration together with those in the electron drift velocity experienced when passing from linearly- to circularly-polarized pumps. Section 3 confirms the previous expectations from a vectorial, $(3 + 1)$ - dimensional (3D) unidirectional pulse propagation model (vectorial UPPE) used to numerically simulate gas jet experiments in argon (short plasma lengths) that preserve the main predictions of the LC model. Section 4 reports experimental data on CP-S, CP-C, LP-O and LP-P using a two-arm setup allowing an individual control of the two colors. Surprisingly, in our setup CP-S pulses produce THz radiation with no particular polarization direction. These unexpected changes are justified by the wide range of values taken by the relative phase of the two colors due to their non-collinear propagation, which also produces ‘young moon’ like field distributions in the THz far field.

2. Plane wave and local-current estimates

To understand the effect of the pump polarization states onto the THz radiated field and energy, we analyze the nonlinear source terms of the medium that can serve as efficient converters into the THz domain. For the sake of simplicity, we shall discard Raman-delayed nonlinearities induced by ro-vibrational transitions of air molecules. As already shown in [50], such nonlinearities are barely influential on the THz performances. We thus consider an instantaneous Kerr response modeling FWM through the associated nonlinear polarization vector:

$$\vec{P}_{\text{Kerr}}(t) = \epsilon_0 \chi^{(3)} E^2(t) \vec{E}(t), \quad (1)$$

where ϵ_0 is the vacuum dielectric constant, $\chi^{(3)}$ the third-order susceptibility defined at the carrier FH frequency $\omega_0 = 2\pi c/\lambda_0$ (c is the speed of light in vacuum), and \vec{E} is the real-valued electric field vector. Besides optical nonlinearities, the plasma response of weakly ionized gases with neutral density N_a is classically modeled by the electron source equation:

$$\partial_t N_e = W(E)(N_a - N_e), \quad (2)$$

where N_e denotes the electron density, $W(E)$ is the ionization rate only depending on the length of the electric field vector $E(t) \equiv |\vec{E}(t)|$. In the present study this rate is given by the instantaneous rate from Ammosov–Delone–Krainov (ADK) theory [51, 52] reducing for hydrogenoid atoms to the well-known quasi-static tunneling (QST) rate [53]:

$$W[E(t)] = \frac{\alpha}{E(t)} e^{-\frac{\beta}{E(t)}}, \quad (3)$$

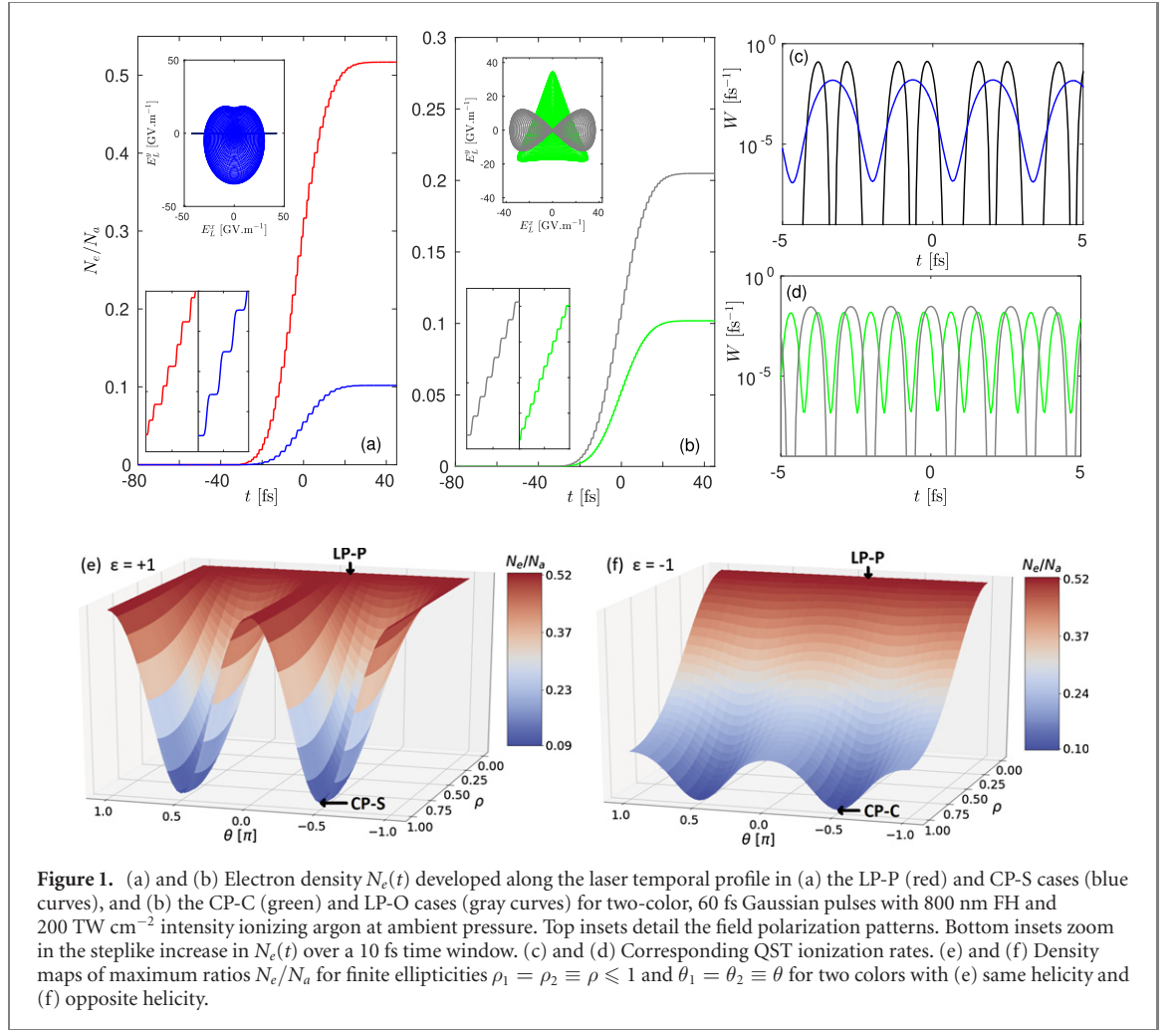
where the constants (α, β) can be found in, e.g., [54].

Without loss of generality, we shall consider a vectorial Gaussian laser field:

$$\vec{E}_L(t) = \sum_{j=1,2} \frac{E_{0j}}{\sqrt{1 + \rho_j^2}} \begin{pmatrix} \cos(j\omega_0 t + \phi_j) \\ \rho_j \cos(j\omega_0 t + \phi_j + \theta_j) \end{pmatrix} e^{-2 \ln 2 \frac{t^2}{\tau_j^2}}, \quad (4)$$

where the small longitudinal component is neglected. The polarization states of FH ($j = 1$) and SH ($j = 2$) field with amplitude E_{0j} are controlled by their respective ellipticities ρ_j and phase angles θ_j . The carrier envelope phase can be set by the phase offsets ϕ_j for each color, while the ratio $r \equiv E_2^2/E_0^2$ denotes the SH intensity fraction with $E_0 = \sqrt{E_1^2 + E_2^2}$ being the overall maximum laser field. The four laser configurations of particular interest are then LP-P: $\rho_j = 0$, CP-S: $\rho_j = 1$, $\theta_j = \pm\pi/2$, CP-C: $\rho_j = 1$, $\theta_1 = -\theta_2 = \pm\pi/2$ and LP-O: $\rho_1 = 0$, $\rho_2 = +\infty$, $\theta_j = 0$. For the sake of conciseness, we shall restrict the phase offsets to $\phi_1 = 0$, $\phi_2 = \phi$ and assume the same full width at half maximum (FWHM) duration $\tau = \tau_j$ for both colors if not stated otherwise. Unless other fractions are addressed, we shall also consider a generic SH intensity fraction of $r = 10\%$ in every pump pulse configuration.

Figure 1 displays illustrative examples of field patterns, ionization yields and QST rates for two-color 60 fs Gaussian pulses with 200 TW cm^{-2} intensity ionizing argon at ambient pressure for the four LP-P,



CP-S, CP-C and LP-O pulses with $\lambda_0 = 800 \text{ nm}$ and relative phase $\phi = \pi/2$ that promotes an optimally-emitting plasma zone in the LP-P case. Higher electron density is reached with a larger field strength for the LP pulses. By contrast, the CP-S pulse develops a lower electron yield through longer and more regular ionization steps lined up on the FH frequency [see figure 1(a), bottom inset and figure 1(c)]. The CP-C pulse induces a 3rd-harmonic periodic growth in the electron density connected to the $3\omega_0$ periodicity of its ionization response [see figure 1(b), bottom inset and figure 1(d)]. The top insets in figure 1 describe the pump field polarization patterns. Note the flattened CP-S contours due to a non-zero SH intensity ratio and the perfect triangular contour of CP-C pulses offering a very symmetric distribution at their field maxima where ionization takes place. As can be seen from figures 1(c) and (d), the ionization rate for Ar never vanishes for CP pulses. Figures 1(e) and (f) detail the density maps for the same intensity value and pulse durations in the further parameter ranges of interest, i.e., $0 \leq \rho_1 = \rho_2 \equiv \rho \leq 1$ and $\theta_1 = \theta_2 \equiv \theta$. These maps reveal important variations in the ionization yield of Ar when modifying the pump polarization states. They will enable us to better appreciate the effective gain in the conversion efficiency achieved when these polarization states are changed.

Discarding the LP-O case (already treated in [31, 45, 48]), we now focus on the LP-P, CP-S and CP-C configurations. For the following analysis the laser field (4) can be simplified by involving a reduced number of parameters as

$$\vec{E}_L(t) = \frac{E_0 e^{-2 \ln 2 \frac{t^2}{\tau^2}}}{\sqrt{1 + \rho^2}} \left[\sqrt{1 - r} \begin{pmatrix} \cos(\omega_0 t) \\ \rho \cos(\omega_0 t + \theta) \end{pmatrix} + \sqrt{r} \begin{pmatrix} \cos(2\omega_0 t + \phi) \\ \rho \epsilon \cos(2\omega_0 t + \theta + \phi) \end{pmatrix} \right]. \quad (5)$$

The LP-P, CP-S and CP-C pump configurations are recovered by simply setting $\rho = 0$, ($\rho = 1, \epsilon = 1, \theta = -\pi/2$) and ($\rho = 1, \epsilon = -1, \theta = -\pi/2$), respectively. Keeping, however, the parameters ρ, θ , and ϵ covering a broader range of values will allow us to study what happens if pump polarizations are imperfect, e.g., a slight ellipticity is introduced.

Let us start our analysis by using simple plane wave arguments, i.e., assuming the limit $\tau \rightarrow +\infty$ in equation (5). First clues on the nonlinear converters' efficiency can be obtained by just looking at the quasi-DC (low-frequency) contributions extracted from the optical or plasma nonlinearities. For CP or LP-P pulses the electric field length expands as

$$E_L(t) = \frac{E_0}{\sqrt{2(1+\rho^2)}} \left\{ 1 + \rho^2 + 2\sqrt{r(1-r)}(1+\epsilon\rho^2)\cos(\omega_0 t + \phi) + (1-\rho^2)(1-r)\cos(2\omega_0 t) \right. \\ \left. + 2\sqrt{r(1-r)}(1-\epsilon\rho^2)\cos(3\omega_0 t + \phi) + (1-\rho^2)r\cos(4\omega_0 t + 2\phi) \right\}^{1/2}, \quad (6)$$

which contains components oscillating at the FH, SH, third and fourth harmonic frequencies. This expression readily leads to the DC Kerr polarization vectors:

$$\vec{P}_{\text{Kerr}}^{\text{LP-P}} = \frac{3\epsilon_0}{4}\chi^{(3)}E_0^3\sqrt{r(1-r)}\begin{pmatrix} \cos\phi \\ 0 \end{pmatrix}, \quad (7)$$

$$\vec{P}_{\text{Kerr}}^{\text{CP}} = \frac{\epsilon_0}{2^{5/2}}\chi^{(3)}E_0^3\sqrt{r(1-r)}(1+\epsilon)\begin{pmatrix} \cos\phi \\ -\sin\phi \end{pmatrix}, \quad (8)$$

indicating that two-color CP pulses may produce a THz radiation being linearly polarized along the angle $-\phi$ when it is driven by the Kerr response only. More involved features can be expected from pulsed beams for which the Kerr-driven THz yield will be evaluated from filtering in frequency the spectrum of $\vec{E}_{\text{Kerr}}^{\text{THz}} \propto \partial_t^2 \vec{P}_{\text{Kerr}}$ [22, 55]. Note that we discarded the factors $(1/3, 2/3)$ affecting n_2 in the cross- and self-phase modulation terms for CP pulses [56, 57], as those will not change the main conclusion below.

On the other hand, to evaluate the efficiency of photocurrents, the THz field \vec{E}_{THz} is extracted according to the LC model [20, 58] by filtering the secondary field $\vec{E}_J = g\partial_t \vec{J}$ emitted from the current density \vec{J} induced by free electrons, g being a geometrical factor originating from Jefimenko's theory [59]. At moderate intensities $< 10^{15}$ W cm $^{-2}$, the temporal shape of \vec{J} is given by the cold-plasma kinetic equation [20]:

$$\partial_t \vec{J} + \nu_c \vec{J} = \frac{e^2}{m_e} N_e \vec{E}, \quad (9)$$

where e and m_e are the electron charge and mass, respectively, and $\nu_c = 2.85$ ps $^{-1}$ denotes the electron-neutral collision rate associated to ~ 350 fs collision time. Following the method exploited in reference [48], the THz waveform follows from the low-frequency (quasi-DC) contribution of the product $N_e(t)\vec{E}(t)$, where $\vec{E}(t) = \vec{E}_L(t)$. The electron density driven by the vectorial laser field (5) can be approximated in the limit $N_e \ll N_a$ and along the slope where $W(E)$ increases with E by $N_e^L(t) \simeq N_a \int_{-\infty}^t W[E_L(t')] dt' \propto \int_{-\infty}^t E_L^2(t') dt'$. Given the electric field length (6), the THz field polarization state estimated from a plane-wave theory expresses in the collisionless limit $\nu_c \rightarrow 0$ as:

$$\vec{E}_{\text{PC}}^{\text{LP-P}} \propto E_0^3 \sqrt{r(1-r)} \begin{pmatrix} \sin\phi \\ 0 \end{pmatrix}, \quad (10)$$

$$\vec{E}_{\text{PC}}^{\text{CP}} \propto E_0^3 \sqrt{r(1-r)}(1+\epsilon) \begin{pmatrix} \sin\phi \\ \cos\phi \end{pmatrix}. \quad (11)$$

The index 'PC' here refers to the photocurrent source. From these expressions, we justify (i) the linear polarization of the THz radiation expected when using CP pump pulses, (ii) the invariance of the THz energy $\propto \int E_{\text{CP}}^2(t') dt'$ with respect to the phase offset ϕ , and (iii) the vanishing of the THz power in the CP-C configuration ($\epsilon = -1$).

For comparison, figures 2(a) and (b) provide a mapping of the maximum-in-time of the Kerr source term filtered in the low-frequency domain $\nu \leq 90$ THz and plotted in the plane (ρ, θ) for 100 TW cm $^{-2}$, 60 fs two-color Gaussian pulses with $\phi = 0$. This intensity value is taken as representative of a transition between Kerr self-focusing and plasma generation in argon along a self-channeling dynamics driven with our laser parameters. Several features emerge from these graphics. First, the Kerr contribution in figure 2 for $\epsilon = 1$ displays similar differences ≈ 2 in the amplitude factors as equations (7) and (8) when comparing Kerr-driven LP-P and CP-S efficiencies [figure 2(a)]. Second, the THz signal is almost extinguished for a CP-C pump pulse [figure 2(b)] as expected from equation (8), the residual noise being attributed to envelope effects. For further comparison, figures 2(c) and (d) display the THz spectra ($\nu \leq 90$ THz) of both Kerr ($\phi = 0$) and photocurrent ($\phi = \pi/2$) source terms for the same pump pulses. One can observe that the photocurrent efficiency is much higher by at least two orders of magnitude than that of the Kerr source in every configuration. This property agrees with current expectations in this intensity range [50]. Since higher intensities will be reached in the coming comprehensive simulations and experiments, we shall henceforth drop the influence of the Kerr response in the following analysis.

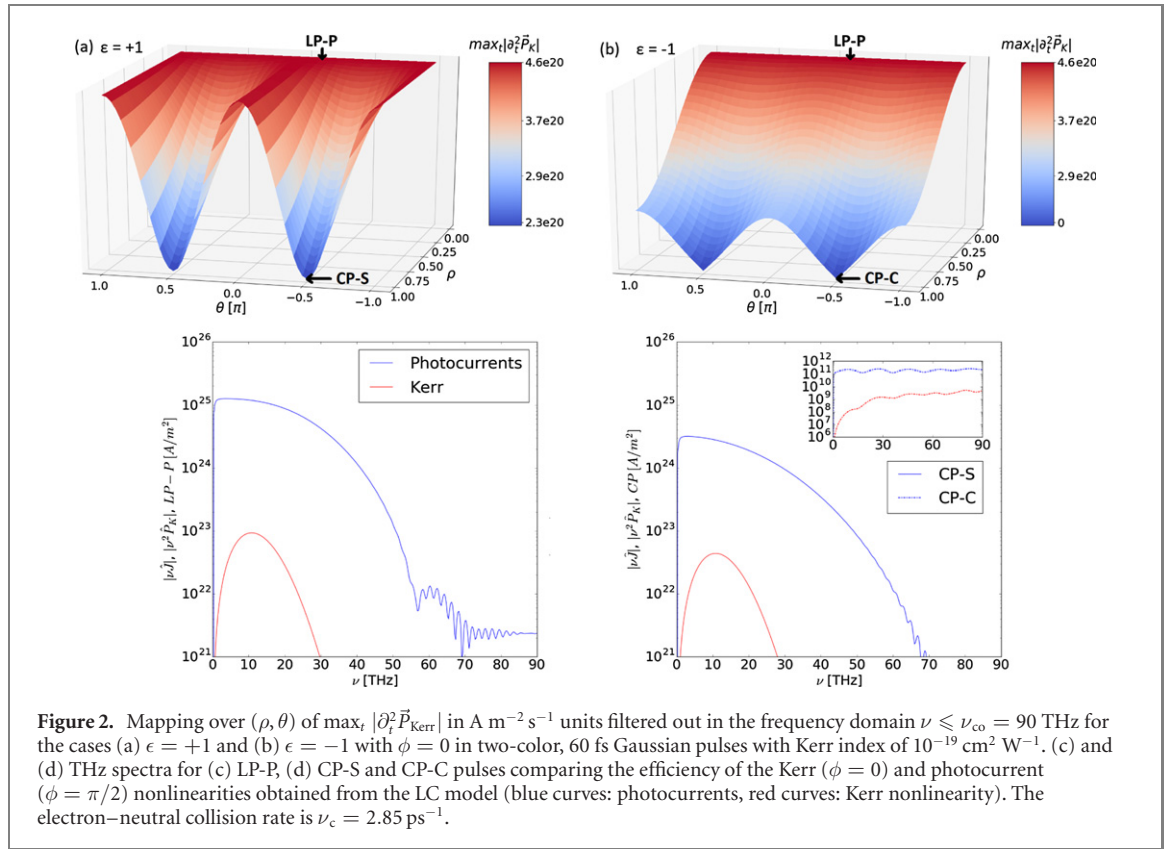


Figure 2. Mapping over (ρ, θ) of $\max_t |\partial_t^2 \vec{P}_{\text{Kerr}}|$ in $\text{A m}^{-2} \text{s}^{-1}$ units filtered out in the frequency domain $\nu \leq \nu_{\text{co}} = 90$ THz for the cases (a) $\epsilon = +1$ and (b) $\epsilon = -1$ with $\phi = 0$ in two-color, 60 fs Gaussian pulses with Kerr index of $10^{-19} \text{ cm}^2 \text{ W}^{-1}$. (c) and (d) THz spectra for (c) LP-P, (d) CP-S and CP-C pulses comparing the efficiency of the Kerr ($\phi = 0$) and photocurrent ($\phi = \pi/2$) nonlinearities obtained from the LC model (blue curves: photocurrents, red curves: Kerr nonlinearity). The electron–neutral collision rate is $\nu_c = 2.85 \text{ ps}^{-1}$.

As highlighted by figures 1(e) and (f) different electron yields are attained when changing the polarization states at constant intensity. To properly apprehend the relative variations in the laser-to-THz conversion efficiency only caused by a change in the pump polarization state, it is more appropriate to remove any related increase in the electron density. Let us recall that, in practical situations, plasma defocusing in three-dimensional propagation geometries usually clamps the achieved peak intensity, which, by feedback, constrains the maximum electron density to comparable levels [50]. Therefore, we henceforth opt for normalizing the THz amplitude $E_{\text{THz}} \propto \partial_t J|_{\text{THz}} \propto N_e^L E_L$ by the asymptotic value of $N_e(t)$ reached at large times. Because the geometrical factor g introduced above is undetermined, we pick it as providing a convenient normalization with respect to the maximum electron density (see also [48]):

$$g = \frac{m_e}{e^2 \max_t N_e^L}. \quad (12)$$

To foresee the best laser configurations, an estimate of the laser-to-THz conversion efficiency is thus defined by

$$\eta_{\text{THz}} \equiv \int_{-\omega_{\text{co}}}^{\omega_{\text{co}}} |\hat{E}_J|^2 d\omega / \int_{-\infty}^{+\infty} |\hat{E}_L|^2 d\omega, \quad (13)$$

where the $\hat{}$ symbol denotes Fourier transform; the numerator is computed in the frequency window $|\omega| \leq \omega_{\text{co}}$ and g is given by equation (12).

Figures 3(a) and (b) show this conversion efficiency, using the laser-gas parameters of figure 1. For comparable electron density levels, maximum generation is reached for CP-S pulses in figure 3(a), as expected. By contrast, CP-C pulses [see figure 3(b)] supply a peculiar configuration extinguishing the THz signal only inside a narrow zone in the plane $\rho \simeq 1, \theta \simeq \pm\pi/2$. A small deviation from this narrow region should thus lead us to recover THz performances comparable with those reached with an LP-P or CP-S state.

To explain the gain in the THz yield when passing from LP-P to CP-S polarization states, we now perform a microscopic description of the photocurrents accounting for the pulsed nature of the laser beams. First, let us observe that, since the ionization rate $W(E)$ only depends on the length of the electric field vector, its extrema are reached at the instants: $\omega_0 t_n \approx n\pi - 2\sqrt{r}(-1)^n \sin \phi / \sqrt{1-r}$ for LP-P beams in the limit $r \ll 1$ [47], $\omega_0 t_n = 2n\pi - \phi$ for CP-S pulses and $\omega_0 t_n = 2n\pi/3 - \phi/3$ for CP-C ones with n being an integer. It is easy to guess from equation (6) that circularly-polarized pulses with same helicity

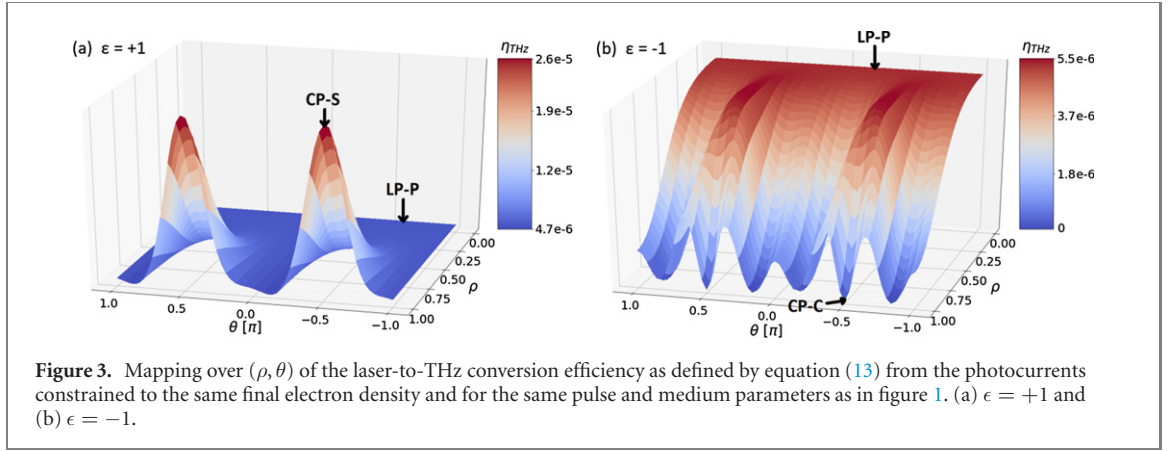


Figure 3. Mapping over (ρ, θ) of the laser-to-THz conversion efficiency as defined by equation (13) from the photocurrents constrained to the same final electron density and for the same pulse and medium parameters as in figure 1. (a) $\epsilon = +1$ and (b) $\epsilon = -1$.

should promote a longer ionization lined up on the FH period alone, unlike the LP pulses that mix up FH and SH frequencies and trigger shorter ionization events.

Following reference [47], we can then sort out the vectorial high-frequency (\vec{J}_A) and low-frequency (\vec{J}_B) current components from equation (9) as $\vec{J}(t) = \vec{J}_A(t) + \vec{J}_B(t)$ with

$$\vec{J}_A(t) = -e \sum_n \delta N_n \vec{v}_f(t) H_n(t - t_n), \quad (14)$$

$$\vec{J}_B(t) = e \sum_n \delta N_n \vec{v}_f(t_n) e^{-\nu_c(t-t_n)} H_n(t - t_n), \quad (15)$$

where δN_n is the elementary ionization step formed at the n th ionization instant, $H_n(t - t_n) = \frac{1}{2}(1 + \text{erf}[(t - t_n)/\tau_n^{\text{ion}}])$ models a steplike function,

$$\tau_n^{\text{ion}} = \sqrt{2} E_L(t_n) / \sqrt{\beta \partial_t^2 E|_{t=t_n}} \quad (16)$$

is the ionization time scale and $\vec{v}_f(t)$ represents the drift velocity in the (x, y) plane of a free electron created at $t = -\infty$:

$$\vec{v}_f(t) = -\frac{e}{m_e} \int_{-\infty}^t \vec{E}_L(t') e^{-\nu_c(t-t')} dt'. \quad (17)$$

Applying the Fourier analysis of reference [32] we extract the radiated field E_f from the frequency window $\nu \leq \nu_{\text{co}} = \omega_{\text{co}}/2\pi$ with $\nu_{\text{co}} = 90$ THz, where the low-frequency radiation is mainly carried out by $\vec{E}_B^{\text{THz}} \propto \partial_t \vec{J}_B|_{\text{THz}}$. This quantity is directly proportional to the kicks in the electron transverse momenta $\propto \vec{v}_f(t_n)$ induced at each ionization event. Expressions of $\vec{v}_f(t_n)$ are detailed in the appendix A. It is found, in particular, that the electron velocity at $t = t_n$ with CP pulses directly depends on the dominant FH amplitude unlike the LP-P pulses fostering a THz field driven by the SH component only. As discussed in appendix A, the SH intensity fraction r must not be too small, for an electron steplike increase to make sense. Under this condition, the electron drift velocity cumulated from all ionization events is higher with CP-S pulses. This difference directly impacts the THz spectrum mainly determined by

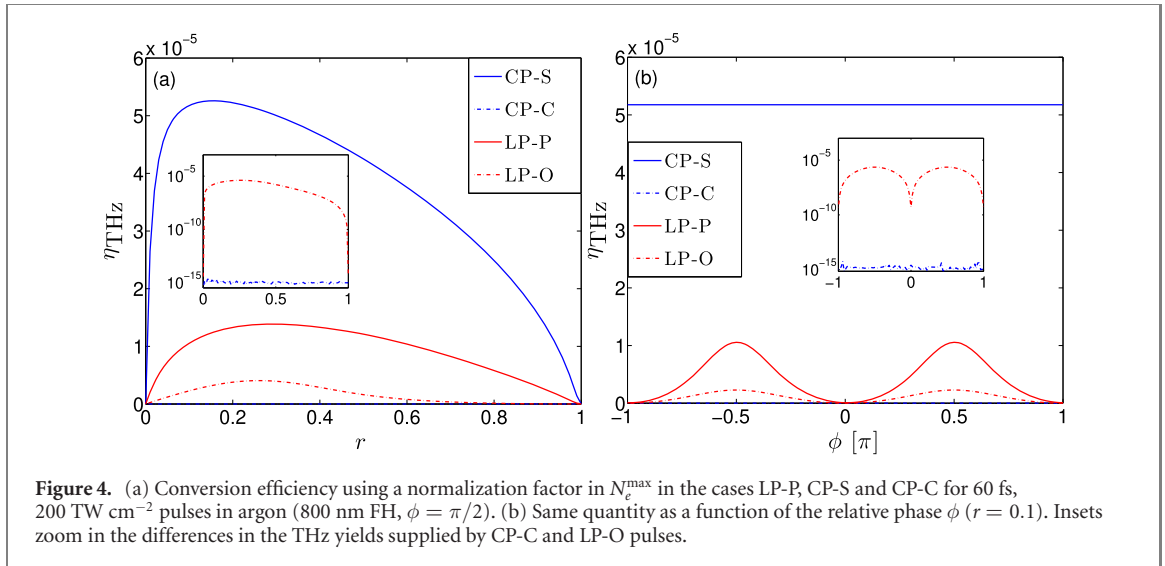
$$\widehat{\vec{E}}^J(\omega) = \frac{ge}{\sqrt{2\pi}} \sum_{n=1}^N \delta N_n \vec{v}_f(t_n) e^{i\omega t_n}, \quad (18)$$

where N denotes the total number of ionization events. Since the elementary density step barely varies with the ionization index n [see figures 1(a) and (b)], we assume $\delta N_n = \delta N$ for all n . Comparing THz fields with equal ionization yield requires to fix the product $N\delta N$ constant for all configurations of interest. Using the above-recalled ionization instants into $\vec{v}_f(t_n)$, the THz spectrum for LP-P pulses expresses, in the limits $\omega/\omega_0 \ll 1$ and $N \gg 1$, as [47]

$$\widehat{E}_{\text{LP-P}}^J(\omega) = \frac{3ge^2 N \delta N E_0}{2\sqrt{2\pi} m_e \omega_0} \sqrt{r} \sin \phi \cos \left(2 \frac{\sqrt{r}}{\sqrt{1-r}} \sin \phi \frac{\omega}{\omega_0} \right) \text{sinc} \left(\frac{N\pi\omega}{2\omega_0} \right). \quad (19)$$

A similar computation enables us to evaluate the THz spectrum for CP-S pulses as

$$\widehat{E}_{\text{CP-S}}^J(\omega) = \frac{ge^2 N \delta N E_0}{2\sqrt{\pi} m_e \omega_0} \left(\sqrt{1-r} + \frac{\sqrt{r}}{2} \right) \text{sinc} \left(\frac{N\pi\omega}{\omega_0} \right) \begin{pmatrix} \sin \phi \\ \cos \phi \end{pmatrix}. \quad (20)$$



From the above expressions, the gain factor at small frequencies $\omega \ll \omega_0$ obtained for CP-S pulses compared to LP-P ones is $G = \frac{\sqrt{2}}{3}(\sqrt{1-r}/\sqrt{r} + 1/2) \approx 1.65$ for $r = 0.1$, i.e., this amplitude gain is close to 2, justifying an increase in the THz power of ~ 4 .

However, the way the THz spectrum builds up for two-color CP-C pulses drastically changes as $\vec{v}_f(t_n)$ now depends on n and leads in the limit $\omega/\omega_0 \rightarrow 0$ to

$$\widehat{E}_{\text{CP-C}}(\omega) \approx \frac{ge^2\delta NE_0}{2\sqrt{\pi}m_e\omega_0} \left(\sqrt{1-r} - \frac{\sqrt{r}}{2} \right) \left(\cos \frac{N\pi}{3} + \frac{1}{\sqrt{3}} \sin \frac{N\pi}{3} \right) \begin{pmatrix} \sin \frac{\phi}{3} \\ \cos \frac{\phi}{3} \end{pmatrix}. \quad (21)$$

The THz yield for CP-C beams is again found to be invariant with the two-color relative phase. Also, whereas this yield directly increases for CP-S pulses from the number of ionization events N , it evolves like $F(N) \equiv \cos(N\pi/3) + \sin(N\pi/3)/\sqrt{3}$ for CP-C ones, which means that their THz field should vanish for pumps containing more than ~ 3 optical cycles. This peculiar property holds due to the perfect periodicity of the CP-C field length in $3\omega_0$.

The validity of the previous LC evaluations has been checked in the appendix (see figure A.1), in particular their agreement with the experimental behaviors of reference [38]. To end this theoretical investigation, figure 4 plots the conversion efficiency, η_{THz} , as a function of the SH intensity fraction r for 200 TW cm⁻², 60 fs two-color Gaussian pulses, demonstrating that the enhancement in the THz field produced by CP-S pulses does depend on this fraction. Figure 4(b) plots the same quantity depending now on the relative phase ϕ between the two colors. One sees, in agreement with the vectorial dependencies (11) and (20), that the THz yields do not vary with ϕ . The insets in figure 4 detail the weak efficiency achieved by the CP-C and LP-O pulses. Note that their respective order of magnitude is reverted compared to the THz powers experimentally reported by Meng *et al* [38]. This difference may be attributed to imperfect CP polarizations (due to, e.g., a slight ellipticity in the experiments). Indeed, a very small departure from an ideal CP-C configuration may lead to a substantial increase in the THz energy, as clearly illustrated by figure 3(b). Note also the sharp slope occurring in the limit $r \rightarrow 0$ for CP pulses, which we relate to the fact that their THz emission is conditioned by the existence of density steps induced by harmonic variations in the ionization rate (see related discussion in appendix A).

3. 3D UPPE simulations of gas jet experiments

The previous properties are now checked by direct 3D numerical computations based on a vectorial version of the unidirectional pulse propagation equation (UPPE) [49, 60] that governs the forward-propagating transverse electric field components E_x, E_y of elliptically-polarized pulses:

$$\partial_z \begin{pmatrix} \hat{E}_x \\ \hat{E}_y \end{pmatrix} = i\sqrt{k^2(\omega) - k_x^2 - k_y^2} \begin{pmatrix} \hat{E}_x \\ \hat{E}_y \end{pmatrix} + i\frac{\mu_0\omega^2}{2k(\omega)} \begin{pmatrix} \hat{\mathcal{F}}_x^{\text{NL}} \\ \hat{\mathcal{F}}_y^{\text{NL}} \end{pmatrix}, \quad (22)$$

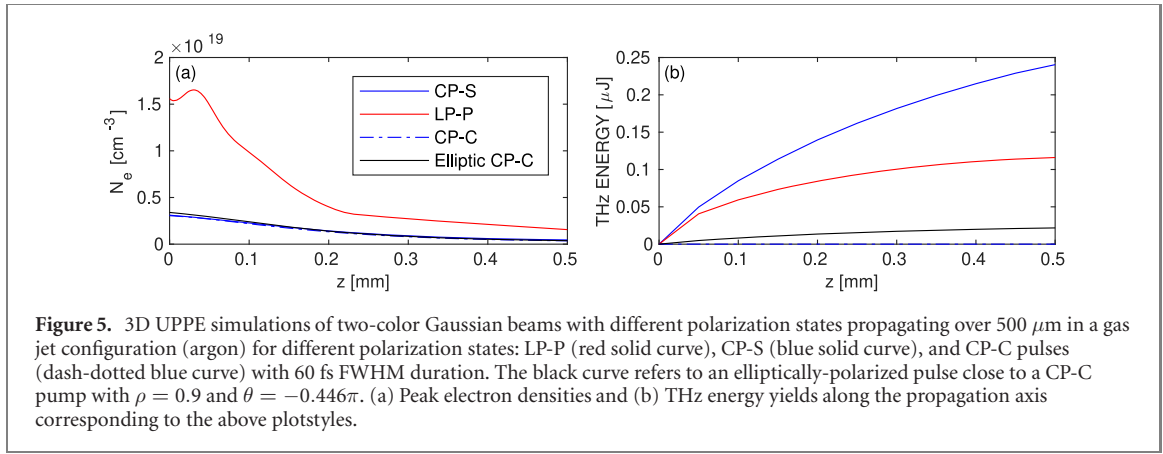
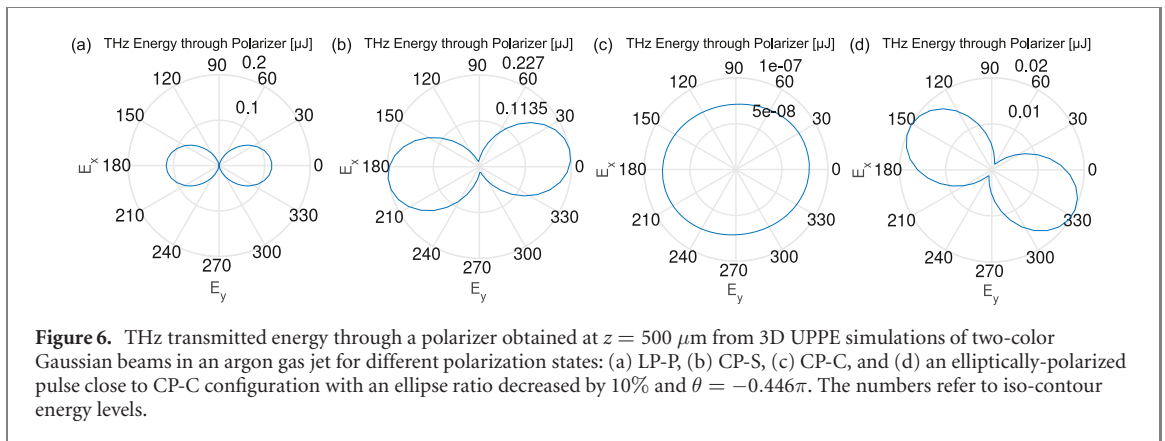


Figure 5. 3D UPPE simulations of two-color Gaussian beams with different polarization states propagating over $500 \mu\text{m}$ in a gas jet configuration (argon) for different polarization states: LP-P (red solid curve), CP-S (blue solid curve), and CP-C pulses (dash-dotted blue curve) with 60 fs FWHM duration. The black curve refers to an elliptically-polarized pulse close to a CP-C pump with $\rho = 0.9$ and $\theta = -0.446\pi$. (a) Peak electron densities and (b) THz energy yields along the propagation axis corresponding to the above plotstyles.

where $\hat{\vec{E}}(k_x, k_y, z, \omega)$ denotes the Fourier transform of the electric field with respect to x , y , and t . As in the previous analysis, the longitudinal electric field component E_z is neglected. The first term on the right-hand side of equation (22) describes linear dispersion and diffraction of the pulse. The term $\hat{\vec{F}}^{\text{NL}} = \hat{\vec{P}}_{\text{Kerr}} + i\hat{\vec{J}}/\omega + i\hat{\vec{J}}_{\text{loss}}/\omega$ contains the third-order nonlinear polarization \vec{P}_{Kerr} given by equation (1) with Kerr index $n_2 = 3\chi^{(3)}/4n_0^2c\epsilon_0$ [$n_0 = n(\omega_0)$], the electron current \vec{J} according to equation (9), and a loss term $\vec{J}_{\text{loss}} = [W(E)(N_a - N_e)U_i/E^2]\vec{E}$ due to ionization [58, 61, 62]. We shall first validate our theoretical expectations using the simple QST model for single-ionized argon (ionization potential $U_i = 15.8$ eV) in the intensity range ~ 200 TW cm^{-2} , in accordance with the laser parameters chosen in the preceding section.

We here simulate gas jet experiments, i.e., setups using micrometer-sized pulse beams propagating over short ranges, $z \leq 500 \mu\text{m}$, in order to limit the linear (diffraction, dispersion) and nonlinear (Kerr response, plasma generation, energy loss) propagation effects that can affect the laser pump components and induce strong variations in their relative phase. Over such short optical paths the pulse intensity (not shown) does not experience strong variations. With an 800 nm FH pump, the two colors have equal input beam width $w_0 = 50 \mu\text{m}$ at $1/e^2$ intensity and FWHM duration of 60 fs. Their peak power is subcritical, $P_{\text{in}} = 0.77P_{\text{cr}}$, with $P_{\text{cr}} \simeq \lambda_0^2/2\pi n_2 = 10.2$ GW and $n_2 = 10^{-19} \text{cm}^2 \text{W}^{-1}$ following [63] for argon at atmospheric pressure. Simulations have been performed using a time window of 0.8 ps, a temporal step of $\Delta t = 50$ attoseconds and transverse resolution of $\Delta x = \Delta y \approx 0.78 \mu\text{m}$. Figure 5 displays the electron density and THz energy yield extracted in the frequency window $\nu \leq \nu_{\text{co}} = 90$ THz for different two-color pump arrangements in LP-P (red solid curve), CP-S and CP-C configurations (solid and dash-dotted blue curves, respectively). The input relative phase between the two colors is set equal to $\pi/2$ and the SH intensity fraction is $r = 10\%$. As seen from figure 5(a), whereas the density created by the CP pulses experiences a smooth attenuation along propagation, that generated by the LP-P pulse undergoes a sharper decrease due to the higher ionization yield enhancing plasma losses. Figure 5(b) reveals the gain in the THz energy yield between CP-S and LP-P reaching a factor ~ 1.44 at $z = 100 \mu\text{m}$ for an electron density ratio between the two pulse configurations of $N_e^{\text{LP-P}}/N_e^{\text{CP-S}} \approx 5$. This gain is even amplified to 2.1 for a density ratio reduced to $N_e^{\text{LP-P}}/N_e^{\text{CP-S}} \approx 3.76$ after $500 \mu\text{m}$ of propagation. Thus, the THz relative gain reported to the same ionization yield is about 7.2–7.9, which reasonably agrees with our LC computations (factor ~ 5 –6, see figures 3 and 4). This gain is all the more important as the electron density decreases in the LP-P configuration and the corresponding THz emission saturates. In addition, the black curve of figure 5 represents the same propagation features for a pump pulse consisting of a perturbed CP-C state with an ellipse ratio reduced by 10% and a relative phase slightly shifted from $\pi/2$ with $\theta = -0.446\pi$. One can observe that perturbing a CP-C state fosters a significant THz emission, which is in agreement with figure 3(b).

Looking further into the THz pulse structure, figure 6 details the THz polarization patterns for the three baseline simulations with $\tau = 60$ fs. As can be seen from figures 6(a) and (b), the CP-S pulse produces a THz polarization pattern being slightly tilted, although the emitted THz field remains mainly polarized along the x axis, as expected from equations (10), (11) and (20) when $\phi = \pi/2$. By contrast, the THz pulse produced by the CP-C pulse does not exceed the background noise level, i.e., no relevant THz waveform is generated, which justifies its isotropic polarization pattern [figure 6(c)]. Figure 6(d) displays the same information for the elliptically-polarized pulse close to a CP-C state, but with an ellipse aspect ratio diminished by 10% and $\theta = -0.446\pi$. We checked that for CP pumps, the polarization ellipse of the emitted THz field is rotated accordingly with the input value of the relative phase ϕ , in accordance with our analytical formulas.

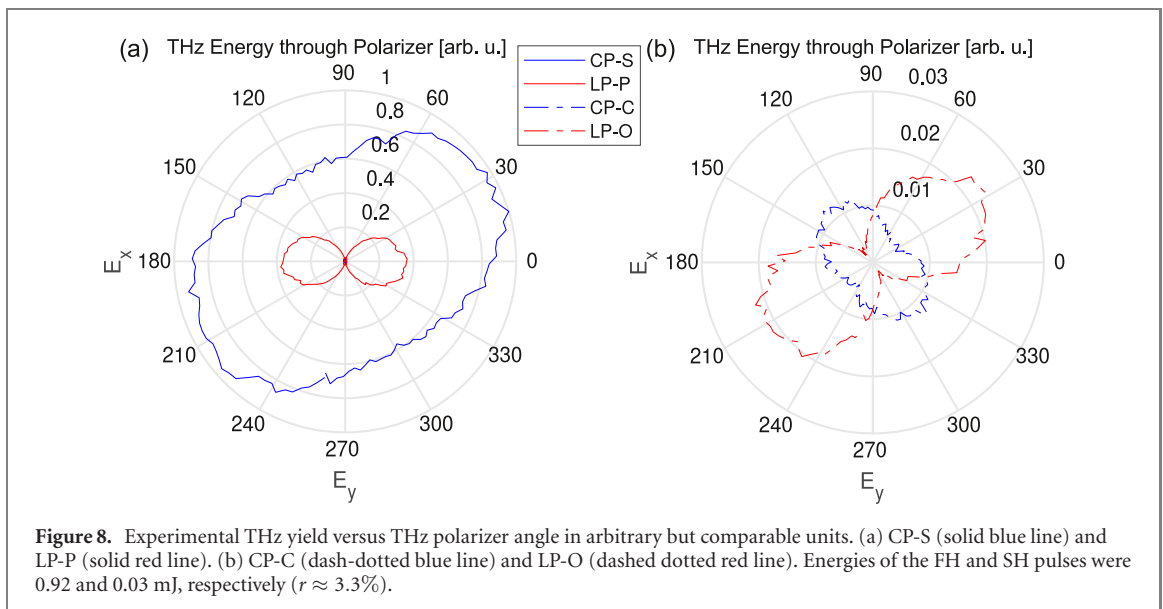
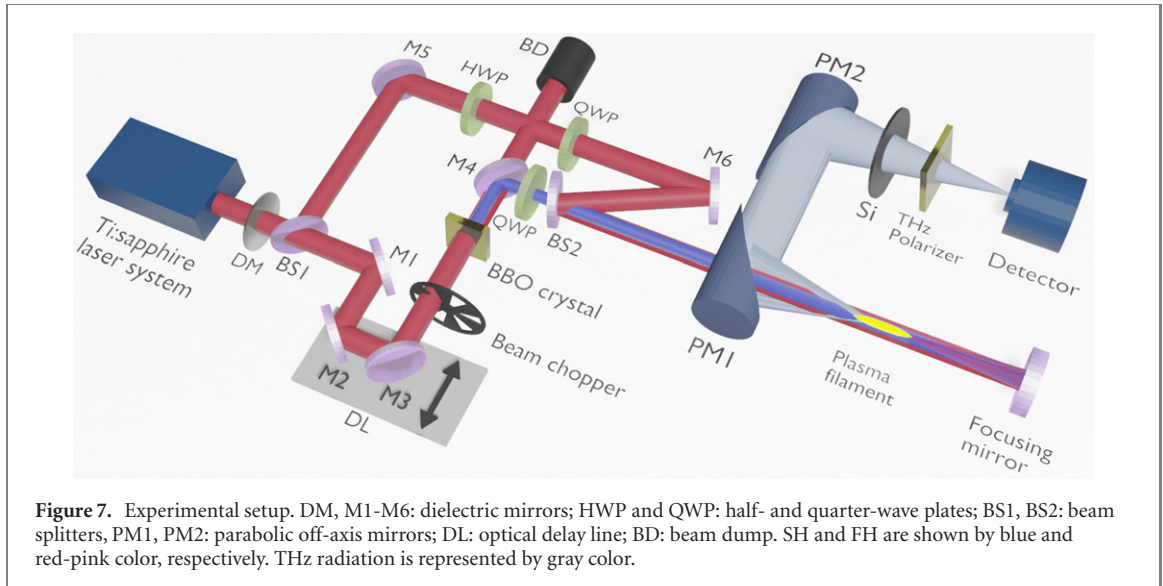


4. Experimental setup and results

THz waves were generated in air by bichromatic femtosecond laser pulses following the setup shown in figure 7. A 1 kHz repetition rate femtosecond Ti:sapphire chirped pulse amplification laser system (Legend elite duo HE+, Coherent Inc.) delivering 40–45 fs (FWHM) light pulses centered at 790 nm with maximal pulse energy of 8 mJ was used as a pump source. The output laser power could be varied by inserting thin partially reflecting dielectric mirrors (DMs) into the beam path. The laser beam was divided into two arms thanks to a thin 50:50 beam splitter (BS1). One of these beams was used for SH generation through a 0.2 mm thick nonlinear BBO crystal. A temporal delay between the FH and SH pulses was introduced by using a motorized optical delay line (DL). The pulse polarization was controlled using broadband zero-order half- and quarter-wave plates (HWP and QWP, respectively) inserted into the beam paths. The QWPs allowed to vary the polarization state of both FH and SH pulses from linear to circular, while HWP inserted into the FH beam path alone was used to switch between the mutually orthogonal and parallel linear polarizations. The FH and SH beams were concentrically superimposed at a dichroic beam splitter (BS2). After passing through the hole of an aluminum-coated off-axis parabolic mirror (PM1) they were directed to a focusing spherical mirror (focal length about 22 cm). As a result, a visible few-mm long plasma filament was produced. In order to minimize optical aberrations the focused bichromatic pump beam was reflected nearly exactly in the backward direction by the focusing mirror. Despite its hole at center, the mirror PM1 was still capable to collect and collimate most of emerging THz radiation, which formed a hollow cone with $\sim 5^\circ$ apex angle [64, 65]. The second parabolic mirror (PM2) then focused the THz beam onto a pyroelectric detector (TPR-A-65 THz, Spectrum Detector Inc.), sensitive in the range 0.1–300 THz ($3000\text{--}1 \mu\text{m}$) with a flat response function from ~ 3 to ~ 100 THz. From FH and SH waves THz radiation was separated by a few 0.5–1 mm-thick high-resistivity silicon wafers. The polarization state of the detected THz beam could be monitored by a broadband high-density polyethylene (HDPE) THz polarizer (Tydex Co.), placed in front of the pyroelectric detector. In order to enhance the detector sensitivity, a lock-in amplifier (SR530, Stanford research systems) along with an optical beam chopper placed into the SH beam path was utilized. To reduce fluctuations of the THz signal the lock-in time constant was kept to be 300 ms in most cases, while the repetition rate of the beam chopper was 5 Hz. Data acquisition and processing was performed by means of a computer and appropriate software, which also controlled parameters of the optical DL and THz polarizer. Imaging of the generated THz beam was performed with a thermal camera detector (VarioCAM head HiRes 640, InfraTec GmbH), sensitive in the range 0.1–40 THz.

Note that, although our experimental setup allowed for an independent control of the intensity, polarization and transverse positions of the focused FH and SH beams, the relative phase between the latter could not be monitored during the experiment, as the system was not interferometrically stabilized. Therefore, the lack of phase stability sometimes resulted in strong fluctuations occurring in the measured THz yields and preventing us from further investigating the influence of the two-color relative phase on the THz generation process. However, our diagnostics were able to average the THz signal over time and consequently, over the relative phase between the FH and SH waves, which allowed us to investigate the main properties of the generated THz radiation as a function of the pump polarization states.

Figure 8 displays the THz yield measured as a function of the THz polarizer (placed in front of the detector) angle for the CP-S, CP-C, LP-P and LP-O pulses with FH and SH pulse energies of 0.92 and 0.03 mJ, respectively. One can see that, in line with our theoretical predictions (see figure 4), the THz yield is the strongest in the CP-S case. A significantly lower THz signal has been obtained from linearly-polarized



pump pulses (lower by a factor of 4.3 and 67 for LP-P and LP-O configurations, respectively). As predicted, the lowest THz yield is obtained for circularly-polarized counterrotating (CP-C) pump waves. Note that, though the numerical analysis indicated that in the CP-C case THz generation could be weaker by about seven orders of magnitude compared with that obtained using LP-O pulses, our experimental THz yield was lower approximately only by a factor ~ 1.4 . This difference can be explained by the fact that it is experimentally quite difficult to produce ideal CP-C pumps, which may significantly rise the efficiency of THz generation. In Meng *et al* experiments [38] the measured THz yield in CP-C case was even higher than that obtained in the LP-O configuration, which could also be explained by non-ideal circularities of the pump polarization states. The fact that slightly perturbed CP-C pulses are able to create a significant THz yield highlights the very peculiar property of ideal CP-C pulses in ‘killing’ THz waves, as justified in section 2. Elliptical pulses departing from an ideal CP-C configuration hence offer a means to trigger moderately small, but non-zero THz powers ranging below the CP-S optimum performances and close to the minimum LP-P conversion efficiencies, as evidenced by figures 3(a) and (b).

Figure 8 also contains partial information on the generated THz polarization state. As expected, for the LP-P pulses THz polarization is clearly linear. An almost linear THz polarization state was also recorded for the LP-O pulses. However, from LC theory one would expect the THz radiation to be polarized like the SH pulse (x -polarized in our experiments). This is obviously not the case, which we attribute to slightly non-orthogonal FH and SH polarization in our experiment. In agreement with observations reported in [44], the LC model predicts that THz polarization is very sensitive to the pump polarization. For example, a

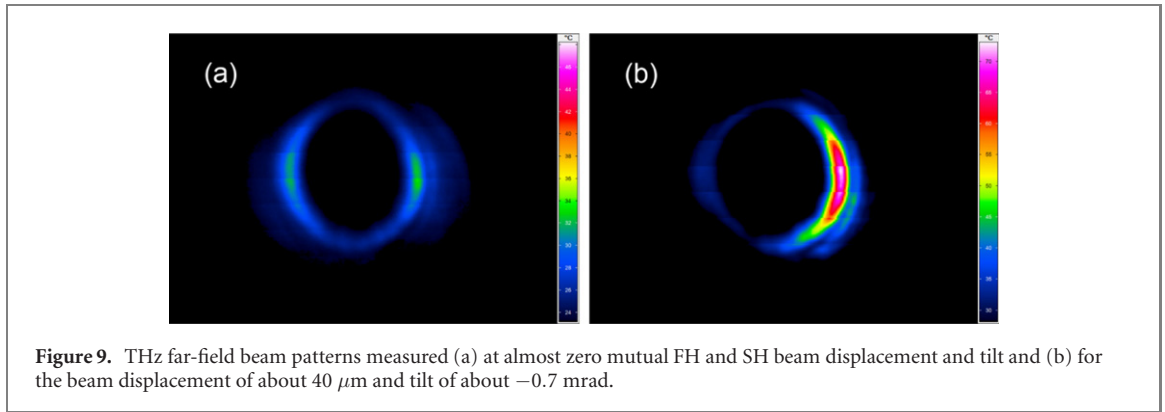


Figure 9. THz far-field beam patterns measured (a) at almost zero mutual FH and SH beam displacement and tilt and (b) for the beam displacement of about $40 \mu\text{m}$ and tilt of about -0.7 mrad .

deviation of only 5 degrees from the ideal 90 degrees is enough to turn the THz polarization by 20 degrees, and sub-optimal phase angle ϕ may render THz polarization even elliptical.

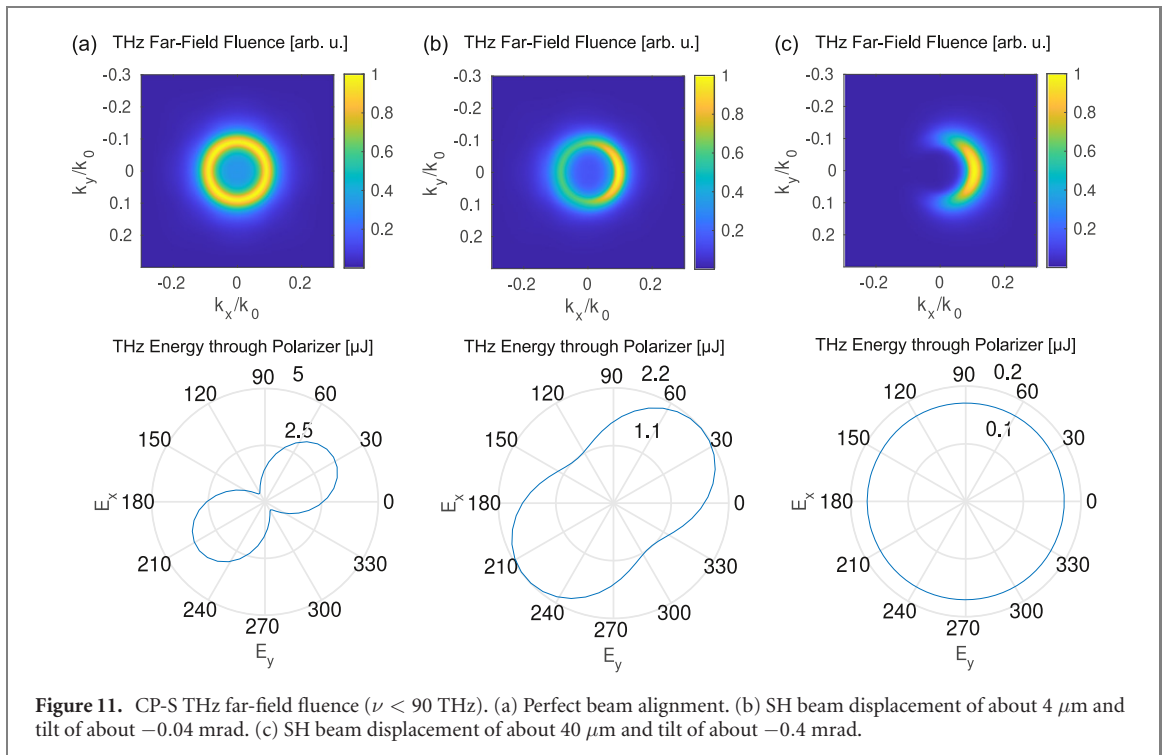
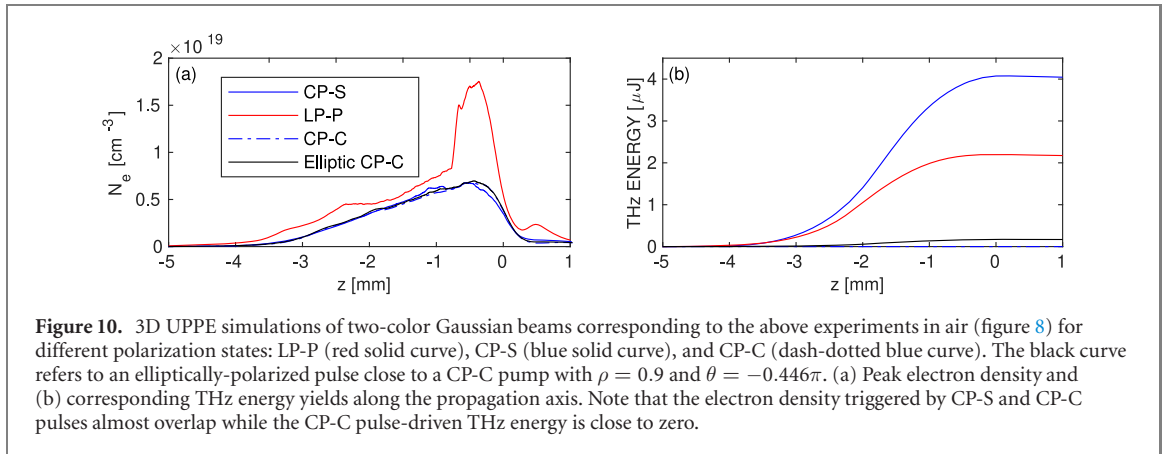
For the CP-S configuration, in contrast to our theoretical predictions, there was only a rather weak dependence in the collected THz signal on the polarizer angle. This rather surprising result could indicate elliptical THz polarization. However, as explained in the next section, this property is caused by imperfect transverse alignment of the two pump colors, in such a way that no THz polarization state can be defined. A larger transverse pump beam displacement and tilt in the focal plane could also significantly modify the spatial intensity distribution of the generated THz radiation. When the beam displacement and tilt were nearly zero, a standard hollow THz cone was produced [see figure 9(a)]. Nonetheless, even slight deviations altering the on-axis, collinear propagation of the two colors resulted in the redistribution of the THz intensity to one side of the beam, creating typically a ‘young moon’ pattern [see figure 9(b)]. Further insight on the polarization state of the radiated field could be gained from measuring the Stokes parameters of the THz radiation, e.g., by using one rotatable THz polarizer in front of a two-contact photoconductive THz detector [66].

5. Role of the transverse shifts in the color alignment

In this final section, the above experimental setup is numerically simulated by means of our 3D UPPE vectorial model. Because experiments were performed in ambient air, we use the effective nonlinear refractive index $n_2 = 1.3 \times 10^{-19} \text{ cm}^2 \text{ W}^{-1}$, mimicking the joint contribution of instantaneous and Raman delayed responses [67, 68] for the sub-50 fs pump-pulses employed here. Linear dispersion of air was taken from [69]. Ionization of both oxygen and nitrogen molecules was taken into account, by employing field-dependent PPT rates for both species and adopting Talebpour *et al* charge numbers $Z_{\text{O}_2}^* = 0.53$, $Z_{\text{N}_2}^* = 0.9$ [70].

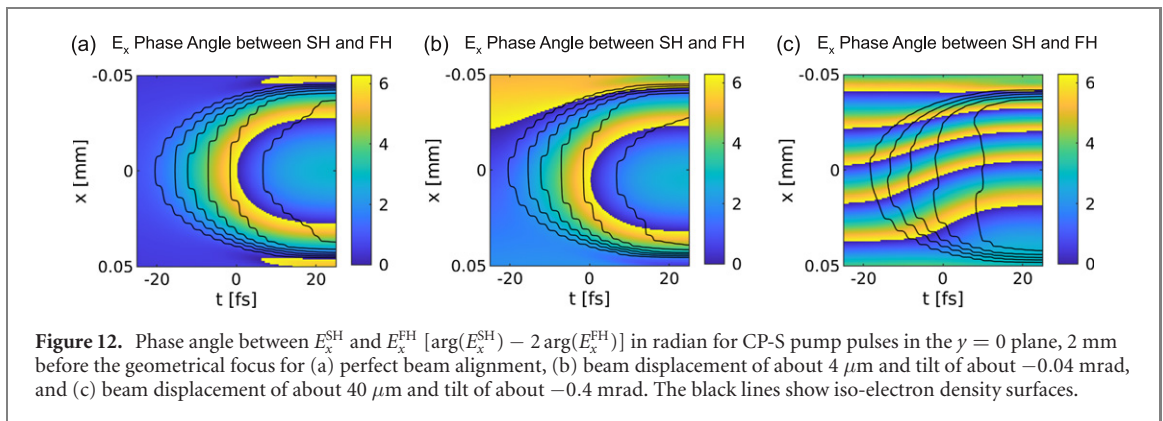
Figure 10 shows results for various pump polarization states and perfect beam alignment. The simulated peak plasma densities in figure 10(a) are comparable for all cases and confirm that a few-mm long plasma is formed before the geometrical focus (here located at $z = 0$). As expected, LP-P pump polarization produces more plasma than CP beams for the same pulse energies and durations. The THz energy produced in the plasma in figure 10(b) confirms once more the impact of the pump polarization as discussed in the previous sections. In order to get significant THz yield from CP-C configuration, a slight ellipticity is required.

Let us now have a closer look at the CP-S case, with particular attention paid to the impact of transverse beam displacements. Figure 11(a) shows the THz far-field fluence pattern in the frequency window $\nu < 90 \text{ THz}$ for perfect beam alignment. As in the experiment, conical THz emission leads to a ring pattern. The THz energy versus polarization indicates almost linear polarization, close to what was observed in the gas-jet simulations of section 3. Due to our two-arm experimental setup, the transverse beam alignment in the focal plane is an issue. In our experimental setup, transverse beam displacement is linked to a tilt angle, which we estimate to $\sim -0.01 \text{ mrad}$ per μm of transverse displacement. This tilt angle can be controlled with a precision of about 0.1 mrad, which translates to an uncertainty of about $\pm 5 \mu\text{m}$ in the transverse relative beam position between FH and SH at focus. Figure 11(b) shows the resulting impact on the far-field fluence pattern for such *small* displacement computed with the UPPE model. The ring pattern is still visible, and compares well to the experimental pattern in figure 9(a). Most importantly, the THz energy distribution versus polarization now agrees with that shown in figure 8(a). This means that a small transverse misalignment of SH and FH, consistent with the limits of our setup, can explain the seemingly elliptical THz polarization observed in our experiments.



On the other hand, *larger* displacements between FH and SH can be introduced deliberately. Such a configuration is shown in figure 11(c), where the transverse displacement is increased by one order of magnitude compared to figure 11(b). A ‘young moon’ pattern is then obtained, comparable to the one shown in figure 9(b). This pattern occurs on the same side to which the SH beam is displaced and directly results from breaking the rotational symmetry. For such large beam displacement, the THz polarization looks completely ‘circular’- or isotropic. We here want to stress that the resulting THz radiation does not have in fact a well-defined polarization state. It just proceeds from a superimposition of THz waves with different polarization states originating from different locations in the plasma, causing the THz energy transmitted through a polarizer to be invariant to the polarizer angle.

As explained in section 2, in CP-S configuration the phase angle ϕ between SH and FH determines the orientation of the (quasi-linearly) polarized THz radiation. Therefore, it is instructive to plot this quantity at a position of strong THz generation inside the plasma. Figure 12 shows the relative phase between the FH and SH components in the plane $y = 0$ for the three pump configurations of figure 11. The first important information is that the relative phase is not constant, but a function of the transverse spatial coordinates and time. Yet, THz radiation can be produced with different polarization states depending on the ionization response along propagation which is directly conditioned by the relative phase locally achieved by the two pump harmonics. Superimposing iso-electron-density lines to the phase plots can thus be instructive. For the perfectly aligned beams in figure 12(a), these iso-electron-density lines follow more or less the phase landscape, so that THz generation favors the standard linear polarization orientation expected in this case,



as observed in figure 11(a). However, already a *small* misalignment of FH and SH beams makes iso-electron-density lines cross regions with significantly varying relative phase, in particular when comparing locations above and below the optical axis. The polarization of the THz waves produced above and below the optical axis differs, which results in an ‘elliptic’ THz polarization shown in figure 11(b). Again, it is important to keep in mind that the resulting THz radiation is *not* strictly speaking elliptically polarized, but it results from a complex spatio-temporal pattern that, once averaged, supplies partially polarized THz light. This assessment is further corroborated by figure 12(c), where due to large beam displacement the iso-electron-density lines and relative phase landscape are completely disconnected. As a result, no preferred direction of polarization is detected by the polarizer in figure 11(c).

We note that other effects may affect the relative phase between FH and SH along the mm-long plasmas and make the THz polarization change along z . Among those effects are the Gouy phases of SH and FH beams, plasma dispersion, as well as slightly different focus positions for SH and FH. Our simulations indicate, however, that the impact of all these effects on the THz polarization is much smaller than that of the above-discussed transverse beam displacements.

6. Conclusion

In this paper, we have investigated the efficiency of the photocurrent mechanism to produce THz pulses when circularly- and elliptically-polarized two color laser pulses are employed. Theoretical evaluations based on plane wave and local current analyses display evidence that a direct dependency of the drift velocity acquired by photo-ionized electrons on the FH pump amplitude and longer ionization sequences explain the increase in the THz power reported by recent experimental and numerical investigations exploiting circularly-polarized two color pulses. When FH and SH pump components counter-rotate, the complete vanishing of the emitted THz radiation has been shown to proceed from destructive interferences linked to the third-harmonic periodicity of the overall laser electric field. Introducing small ellipticity may, by contrast, allow to recover relevant THz energies. These results have been confirmed by direct full (3D + 1) UPPE simulations of short, gas-jet plasmas.

In addition, our experimental measurements using a two-armed setup recovered the main trends on THz generation efficiencies for linearly- and circularly-polarized pump pulses over longer (mm-long) plasma-filament ranges. However, our THz polarization measurements did not confirm the occurrence of linearly-polarized THz fields predicted by our theoretical findings, but instead some undefined polarization state, with either elliptical or even circular energy distribution. Comprehensive 3D simulations revealed that such polarization patterns occur due to slight transverse beam displacements and tilts of the pump harmonics in the focal plane, which causes generation of THz waves with different polarization orientations that superimpose. This insight is of crucial importance for applications sensitive to the THz polarization state. We expect that our results will pave the way toward more performant and stable broadband THz sources, and will trigger future experiments in this field.

Acknowledgments

This work was supported by the ANR/MATURATION Project ‘ALTESSE 2’ # ANR-19-ASMA-0007 and by the Agence Innovation Défense. It was performed using HPC resources from GENCI (Grant # A0080507594). DB and VV acknowledge the Research Council of Lithuania for funding this research by the

Grant # S-MIP-19-46 and support from the Laserlab-Europe EU-H2020 871124. SS acknowledges support by the Qatar National Research Fund through the National Priorities Research Program (Grant # NPRP 12S-0205-190047). IB is thankful for support from the Deutsche Forschungsgemeinschaft (DFG BA4156/4-2) and from the German Research Foundation under Germany's Excellence Cluster PhoenixD (EXC 2122 Project ID 390833453).

Appendix A. Calculation of electron drift velocities and LC results

Assuming long enough pulses to treat them with slowly varying envelope, equation (17) can be expanded as

$$\vec{v}_f(t) \simeq -\frac{eE_0 e^{-2\ln 2 \frac{t^2}{\tau^2}}}{m_e \sqrt{1+\rho^2}} \left(\frac{\sqrt{1-r}[\nu_c \cos(\omega_0 t) + \omega_0 \sin(\omega_0 t)]}{\nu_c^2 + \omega_0^2} + \frac{\sqrt{r}[\nu_c \cos(2\omega_0 t + \phi) + 2\omega_0 \sin(2\omega_0 t + \phi)]}{\nu_c^2 + 4\omega_0^2} \right. \\ \left. + \frac{\rho\sqrt{1-r}[\nu_c \cos(\omega_0 t + \theta) + \omega_0 \sin(\omega_0 t + \theta)]}{\nu_c^2 + \omega_0^2} + \frac{\rho e\sqrt{r}[\nu_c \cos(2\omega_0 t + \theta + \phi) + 2\omega_0 \sin(2\omega_0 t + \theta + \phi)]}{\nu_c^2 + 4\omega_0^2} \right). \quad (\text{A.1})$$

This expression directly provides the drift electron velocities evaluated at $t = t_n$ for a collisionless plasma ($\nu_c \rightarrow 0$) and assuming $r \ll 1$, namely,

$$v_f^{\text{LP-P}}(t_n) = 3eE_0\sqrt{r} \sin \phi / (2m_e\omega_0), \quad (\text{A.2})$$

$$\vec{v}_f^{\text{CP-S}}(t_n) = \frac{eE_0}{\sqrt{2}m_e\omega_0} \left(\sqrt{1-r} + \frac{\sqrt{r}}{2} \right) \begin{pmatrix} \sin \phi \\ \cos \phi \end{pmatrix}, \quad (\text{A.3})$$

and

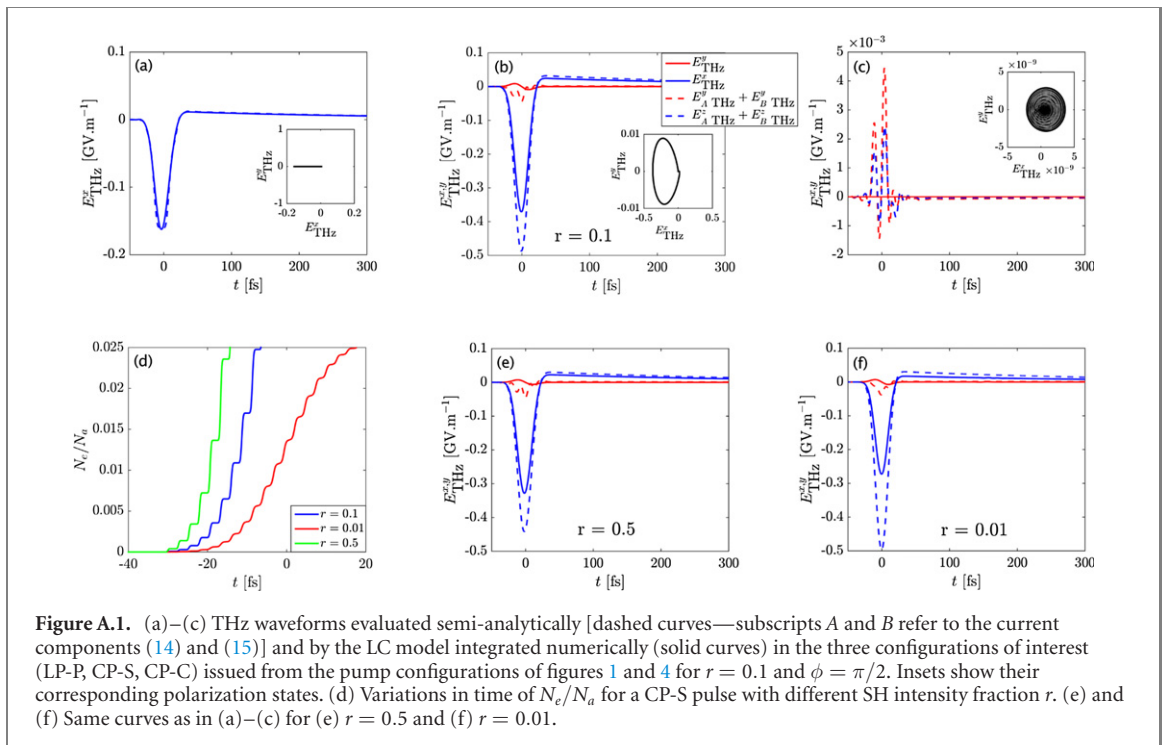
$$\vec{v}_f^{\text{CP-C}}(t_n) = \frac{eE_0}{\sqrt{2}m_e\omega_0} \left(\sqrt{1-r} - \frac{\sqrt{r}}{2} \right) \begin{pmatrix} \sin(\phi/3 - 2n\pi/3) \\ \cos(\phi/3 - 2n\pi/3) \end{pmatrix}, \quad (\text{A.4})$$

for the LP-P, CP-S and CP-C pump configurations associated with the ionization instants $\omega_0 t_n^{\text{LP-P}} \approx n\pi - 2\sqrt{r}(-1)^n \sin \phi / \sqrt{1-r}$, $\omega_0 t_n^{\text{CP-S}} = 2n\pi - \phi$ and $\omega_0 t_n^{\text{CP-C}} = 2n\pi/3 - \phi/3$, respectively.

The information gained through this microscopic description is the direct dependency of the electron velocity (A.3) on the dominant FH amplitude and not on the SH one as is the case of LP-P pulses. Note that, for LP-P pulses and CP-S pulses as well, the kick in the electron momenta $\propto \vec{v}_f(t_n)$ is here independent on the ionization instant n , so that the THz spectrum (18) proceeds from the sum $\sum_n e^{i\omega t_n}$ only.

It is worth emphasizing that, in the present analysis, $\vec{v}_f(t_n)$ does not reduce to zero for CP pulses in the limit of no SH ($r \rightarrow 0$). In this limit, the emitted THz field should, however, vanish, as shown in figure 4(a). This behavior follows from the fact that the absence of SH color limits the ionization yield to a smooth increase in the electron density that just follows the envelope of the FH pulse. Reversely, our microscopic model is based on a steplike increase in the density, which can only be realized through the existence of short ionization instants compared to the width of the density steps, typically $\tau_n^{\text{ion}} \ll \Delta t_n = t_{n+1} - t_n$. A straightforward manipulation of equation (16) together with equation (6) leads to the diverging behavior $\tau_n^{\text{ion}} \simeq 2^{1/4} \sqrt{E_0/\beta} (\omega_0 r^{1/4})^{-1}$ in the limit of small r , so that, e.g., the requirement $\tau_n^{\text{ion}} \leq \Delta t_n/10 = \pi/5\omega_0$ for CP-S pulses supplies the minimum bound $r \geq r_{\text{lim}} = 10^4 E_0^2 / (8\pi^4 \beta^2)$. Therefore, for CP pump pulses equations (20) and (21) are only valid for large enough SH intensity fraction r . For smaller r , and therefore longer ionization events, electrons born at different times than t_n start to contribute to the current. Because their trajectory is different, they do not contribute to the low frequency component emitting the THz radiation; in the worst case they may even produce a current with opposite sign, reducing thereby the radiation yield.

Figures A.1(a)–(c) illustrate the on-axis field components (dashed curves) expected from the current components (14) and (15) for the same Gaussian pulses as in figure 4. Compared with LP-P pulses the THz waveform computed over the frequency range $\nu \leq 90$ THz and generated over the laser region ($|t| \leq 60$ fs) is higher in CP-S configuration by a factor 3. CP-C-driven THz waveforms appear negligible. These results qualitatively agree with those of the LC model numerically integrated from equation (9) (solid curves) and providing a factor ~ 2.3 in the CP-S field strength, thus a factor ~ 5 in its THz power, which is consistent with [38]. As previously mentioned, discrepancies in the CP configurations are due to an overestimation of the photocurrent efficiency over a full electron density step δN . Such discrepancies are, however, quite limited for high enough values of $r \geq 0.1$. The insets detail the resulting polarization states, remaining linear in LP-P, but becoming slightly elliptical when they are driven by photocurrents as reported in [40]. Departing from both equations (11) and (20), this slight ellipticity in the CP-S case results from the pulse envelope and the finite duration of the ionization events (small rotation of the polarization ellipse). For comparison, figures A.1(d)–(f) show the evolution in the electron density steps and THz pulse components for CP-S pulses with different intensity ratios $r = 0.01, 0.1, 0.5$. We can observe that the agreement between



the semi-analytical and numerical computation of the THz pulse components becomes degraded when the value of r is decreased to zero.

ORCID iDs

S Skupin <https://orcid.org/0000-0002-9215-1150>

I Babushkin <https://orcid.org/0000-0001-9686-0811>

V Vaičaitis <https://orcid.org/0000-0002-9084-8552>

L Bergé <https://orcid.org/0000-0002-5531-7692>

References

- [1] Tonouchi M 2007 Cutting-edge terahertz technology *Nat. Photon.* **1** 97
- [2] Wallace V P, Taday P F, Fitzgerald A J, Woodward R M, Cluff J, Pye R J and Arnone D D 2004 Terahertz pulsed imaging and spectroscopy for biomedical and pharmaceutical applications *Faraday Discuss.* **126** 255
- [3] Jepsen P U, Cooke D G and Koch M 2011 Terahertz spectroscopy and imaging—modern techniques and applications *Laser Photon. Rev.* **5** 124
- [4] Bergé L et al 2019 Terahertz spectroscopy from air plasmas created by two-color femtosecond laser pulses: the ALTESSE project *Europhys. Lett.* **126** 24001
- [5] Curcio A, Marocchino A, Dolci V, Lupi S and Petrarca M 2018 Resonant plasma excitation by single-cycle THz pulses *Sci. Rep.* **8** 1052
- [6] LaRue J L, Katayama T, Lindenberg A, Fisher A S, Öström H, Nilsson A and Ogasawara H 2015 THz-pulse-induced selective catalytic CO oxidation on Ru *Phys. Rev. Lett.* **115** 036103
- [7] Hamster H, Sullivan A, Gordon S, White W and Falcone R W 1993 Subpicosecond, electromagnetic pulses from intense laser–plasma interaction *Phys. Rev. Lett.* **71** 2725–8
- [8] Leemans W P et al 2003 Observation of terahertz emission from a laser–plasma accelerated electron bunch crossing a plasma–vacuum boundary *Phys. Rev. Lett.* **91** 074802
- [9] Déchard J, Debayle A, Davoine X, Gremillet L and Bergé L 2018 Terahertz pulse generation in underdense relativistic plasmas: from photoionization-induced radiation to coherent transition radiation *Phys. Rev. Lett.* **120** 144801
- [10] Suen J Y, Li W, Taylor Z D and Brown E R 2010 Characterization and modeling of a terahertz photoconductive switch *Appl. Phys. Lett.* **96** 141103
- [11] Ropagnol X et al 2016 Intense THz pulses with large ponderomotive potential generated from large aperture photoconductive antennas *Opt. Express* **24** 11299
- [12] Bachmann D, Rösch M, Süess M J, Beck M, Unterrainer K, Darmo J, Faist J and Scalari G 2016 Short pulse generation and mode control of broadband terahertz quantum cascade lasers *Optica* **3** 1087
- [13] Vicario C, Monoszlai B and Hauri C P 2014 GV/m single-cycle terahertz fields from a laser-driven large-size partitioned organic crystal *Phys. Rev. Lett.* **112** 213901
- [14] Fülöp J A, Ollmann Z, Lombosi C, Skrobel C, Klingebiel S, Pálfalvi L, Krausz F, Karsch S and Hebling J 2014 Efficient generation of THz pulses with 04 mJ energy *Opt. Express* **22** 20155

- [15] Jang D, Schwartz R M, Woodbury D, Griff-McMahon J, Younis A H, Milchberg H M and Kim K-Y 2019 Efficient terahertz and Brunel harmonic generation from air plasma via mid-infrared coherent control *Optica* **6** 1338
- [16] Koulouklidis A D, Gollner C, Shumakova V, Fedorov V Y, Pugžlys A, Baltuška A and Tzortzakis S 2020 Observation of extremely efficient terahertz generation from mid-infrared two-color laser filaments *Nat. Commun.* **11** 292
- [17] Cook D J and Hochstrasser R M 2000 Intense terahertz pulses by four-wave rectification in air *Opt. Lett.* **25** 1210
- [18] Kress M, Löffler T, Eden S, Thomson M and Roskos H G 2004 Terahertz-pulse generation by photoionization of air with laser pulses composed of both fundamental and second-harmonic waves *Opt. Lett.* **29** 1120
- [19] Oh T I, You Y S, Jhaji N, Rosenthal E W, Milchberg H M and Kim K Y 2013 Intense terahertz generation in two-color laser filamentation: energy scaling with terawatt laser systems *New J. Phys.* **15** 075002
- [20] Kim K Y, Taylor A J, Glowina J H and Rodriguez G 2008 Coherent control of terahertz supercontinuum generation in ultrafast laser-gas interactions *Nat. Photon.* **2** 605
- [21] Kim K-Y, Glowina J H, Taylor A J and Rodriguez G 2007 Terahertz emission from ultrafast ionizing air in symmetry-broken laser fields *Opt. Express* **15** 4577
- [22] Bergé L, Skupin S, Köhler C, Babushkin I and Herrmann J 2013 3D numerical simulations of THz generation by two-color laser filaments *Phys. Rev. Lett.* **110** 073901
- [23] Li M, Li W, Shi Y, Lu P, Pan H and Zeng H 2012 Verification of the physical mechanism of THz generation by dual-color ultrashort laser pulses *Appl. Phys. Lett.* **101** 161104
- [24] Clerici M et al 2013 Wavelength scaling of terahertz generation by gas ionization *Phys. Rev. Lett.* **110** 253901
- [25] Nguyen A et al 2019 Wavelength scaling of terahertz pulse energies delivered by two-color air plasmas *Opt. Lett.* **44** 1844
- [26] Fedorov V Y and Tzortzakis S 2018 Optimal wavelength for two-color filamentation-induced terahertz sources *Opt. Express* **26** 31150
- [27] Nguyen A, González de Alaiza Martínez P, Thiele I, Skupin S and Bergé L 2018 Broadband terahertz radiation from two-color mid- and far-infrared laser filaments in air *Phys. Rev. A* **97** 063839
- [28] Debayle A, González de Alaiza Martínez P, Gremillet L and Bergé L 2015 Non-monotonic increase in laser-driven THz emissions through multiple ionization events *Phys. Rev. A* **91** 041801
- [29] Thiele I, Nuter R, Bousquet B, Tikhonchuk V, Skupin S, Davoine X, Gremillet L and Bergé L 2016 Theory of terahertz emission from femtosecond-laser-induced microplasmas *Phys. Rev. E* **94** 063202
- [30] Buccheri F and Zhang X-C 2015 Terahertz emission from laser-induced microplasma in ambient air *Optica* **2** 366
- [31] Thiele I, González de Alaiza Martínez P, Nuter R, Nguyen A, Bergé L and Skupin S 2017 Broadband terahertz emission from two-color femtosecond-laser-induced microplasmas *Phys. Rev. A* **96** 053814
- [32] González de Alaiza Martínez P, Babushkin I, Bergé L, Skupin S, Cabrera-Granado E, Köhler C, Morgner U, Husakou A and Herrmann J 2015 Boosting terahertz generation in laser-field ionized gases using a sawtooth wave shape *Phys. Rev. Lett.* **114** 183901
- [33] Zhou B, Wang Y, Hong L, Mahdi D and Jepsen P U 2018 High-efficiency sub-single-cycle THz wave generation by three color air plasma *2018 43rd Int. Conf. Infrared, Millimeter and Terahertz Waves (IRMMW-THz)* (IEEE) p 1
- [34] Vaičaitis V, Balachninaïtė O, Morgner U and Babushkin I 2019 Terahertz radiation generation by three-color laser pulses in air filament *J. Appl. Phys.* **125** 173103
- [35] Zhang L-L, Wang W-M, Wu T, Zhang R, Zhang S-J, Zhang C-L, Zhang Y, Sheng Z-M and Zhang X-C 2017 Observation of terahertz radiation via the two-color laser scheme with uncommon frequency ratios *Phys. Rev. Lett.* **119** 235001
- [36] Wang W-M, Sheng Z-M, Li Y-T, Zhang Y and Zhang J 2017 Terahertz emission driven by two-color laser pulses at various frequency ratios *Phys. Rev. A* **96** 023844
- [37] Dai J, Karpowicz N and Zhang X-C 2009 Coherent polarization control of terahertz waves generated from two-color laser-induced gas plasma *Phys. Rev. Lett.* **103** 023001
- [38] Meng C, Chen W, Wang X, Lü Z, Huang Y, Liu J, Zhang D, Zhao Z and Yuan J 2016 Enhancement of terahertz radiation by using circularly polarized two-color laser fields *Appl. Phys. Lett.* **109** 131105
- [39] Yuan K-J and Bandrauk A D 2011 Angle-dependent molecular above-threshold ionization with ultrashort intense linearly and circularly polarized laser pulses *Phys. Rev. A* **84** 013426
- [40] Fedorov V Y, Koulouklidis A D and Tzortzakis S 2017 THz generation by two-color femtosecond filaments with complex polarization states: four-wave mixing versus photocurrent contributions *Plasma Phys. Control. Fusion* **59** 014025
- [41] Song L, Bai Y, Xu R, Li C, Liu P, Li R and Xu Z 2013 Polarization control of terahertz waves generated by circularly polarized few-cycle laser pulses *Appl. Phys. Lett.* **103** 261102
- [42] You Y S, Oh T I and Kim K-Y 2013 Mechanism of elliptically polarized terahertz generation in two-color laser filamentation *Opt. Lett.* **38** 1034
- [43] Yousef-Zamanian A and Neshat M 2017 Investigation of polarization state of terahertz radiation from compact laser-induced plasma in air *J. Mod. Opt.* **64** 300
- [44] Kosareva O et al 2018 Polarization control of terahertz radiation from two-color femtosecond gas breakdown plasma *Opt. Lett.* **43** 90
- [45] Esaulkov M, Kosareva O, Makarov V, Panov N and Shkurinov A 2015 Simultaneous generation of nonlinear optical harmonics and terahertz radiation in air: polarization discrimination of various nonlinear contributions *Front. Optoelectron.* **8** 73
- [46] Tulskey V A, Bagheri M, Saalman U and Popruzhenko S V 2018 Boosting terahertz-radiation power with two-color circularly polarized midinfrared laser pulses *Phys. Rev. A* **98** 053415
- [47] Babushkin I, Skupin S, Husakou A, Köhler C, Cabrera-Granado E, Bergé L and Herrmann J 2011 Tailoring terahertz radiation by controlling tunnel photoionization events in gases *New J. Phys.* **13** 123029
- [48] Nguyen A, González de Alaiza Martínez P, Thiele I, Skupin S and Bergé L 2018 THz field engineering in two-color femtosecond filaments using chirped and delayed laser pulses *New J. Phys.* **20** 033026
- [49] Kolesik M and Moloney J V 2004 Nonlinear optical pulse propagation simulation: from Maxwell's to unidirectional equations *Phys. Rev. E* **70** 036604
- [50] Nguyen A, González de Alaiza Martínez P, Déchard J, Thiele I, Babushkin I, Skupin S and Bergé L 2017 Spectral dynamics of THz pulses generated by two-color laser filaments in air: the role of Kerr nonlinearities and pump wavelength *Opt. Express* **25** 4720
- [51] Ammosov M V, Delone N B and Kraïnov V P 1986 Tunnel ionization of complex atoms and of atomic ions in an alternating electromagnetic field *Sov. Phys. JETP* **64** 1191

- [52] Thomson M D, Kress M, Löffler T and Roskos H G 2007 Broadband THz emission from gas plasmas induced by femtosecond optical pulses: from fundamentals to applications *Laser Photon. Rev.* **1** 349
- [53] Landau L D and Lifshitz E M 1965 *Quantum Mechanics* (Oxford: Pergamon)
- [54] González de Alaiza Martínez P and Bergé L 2014 Influence of multiple ionization in laser filamentation *J. Phys. B: At. Mol. Opt. Phys.* **47** 204017
- [55] Borodin A V, Panov N A, Kosareva O G, Andreeva V A, Esaulkov M N, Makarov V A, Shkurinov A P, Chin S L and Zhang X-C 2013 Transformation of terahertz spectra emitted from dual-frequency femtosecond pulse interaction in gases *Opt. Lett.* **38** 1906
- [56] Agrawal G P 2001 *Nonlinear Fiber Optics* 3rd edn (New York: Academic)
- [57] Bergé L, Gouédard C, Schjodt-Eriksen J and Ward H 2003 Filamentation patterns in Kerr media vs. beam shape robustness, nonlinear saturation and polarization states *Physica D* **176** 181
- [58] Babushkin I, Kuehn W, Köhler C, Skupin S, Bergé L, Reimann K, Woerner M, Herrmann J and Elsaesser T 2010 Ultrafast spatiotemporal dynamics of terahertz generation by ionizing two-color femtosecond pulses in gases *Phys. Rev. Lett.* **105** 053903
- [59] Jefimenko O D 1966 *Electricity and Magnetism: An Introduction to the Theory of Electric and Magnetic Fields* (New York: Appleton-Century-Crofts)
- [60] Kolesik M, Moloney J V and Mlejnek M 2002 Unidirectional optical pulse propagation equation *Phys. Rev. Lett.* **89** 283902
- [61] Bergé L, Skupin S, Nuter R, Kasparian J and Wolf J-P 2007 Ultrashort filaments of light in weakly ionized, optically transparent media *Rep. Prog. Phys.* **70** 1633
- [62] Bergé L and Skupin S 2008 Few-cycle light bullets created by femtosecond filaments *Phys. Rev. Lett.* **100** 113902
- [63] Loriot V, Hertz E, Faucher O and Lavorel B 2009 Measurement of high order Kerr refractive index of major air components *Opt. Express* **17** 13429
- [64] Zhong H, Karpowicz N and Zhang X-C 2006 Terahertz emission profile from laser-induced air plasma *Appl. Phys. Lett.* **88** 261103
- [65] Vaičaitis V, Ivanov M, Adomavičius K, Svirskas Ž, Morgner U and Babushkin I 2018 Influence of laser-preformed plasma on THz wave generation in air by bichromatic laser pulses *Laser Phys.* **28** 095402
- [66] Dong H, Gong Y and Olivo M 2010 Measurement of Stokes parameters of terahertz radiation in terahertz time-domain spectroscopy *Microw. Opt. Technol. Lett.* **52** 2319
- [67] Wahlstrand J K, Cheng Y H and Milchberg H M 2012 Absolute measurement of the transient optical nonlinearity in N₂, O₂, N₂O, and Ar *Phys. Rev. A* **85** 043820
- [68] Rosenthal E W, Palastro J P, Jhajj N, Zahedpour S, Wahlstrand J K and Milchberg H M 2015 Sensitivity of propagation and energy deposition in femtosecond filamentation to the nonlinear refractive index *J. Phys. B: At. Mol. Opt. Phys.* **48** 094011
- [69] Peck E R and Reeder K 1972 Dispersion of air. *J. Opt. Soc. Am.* **62** 958
- [70] Talebpour A, Yang J and Chin S L 1999 Semi-empirical model for the rate of tunnel ionization of N₂ and O₂ molecule in an intense Ti:sapphire laser pulse *Opt. Commun.* **163** 29